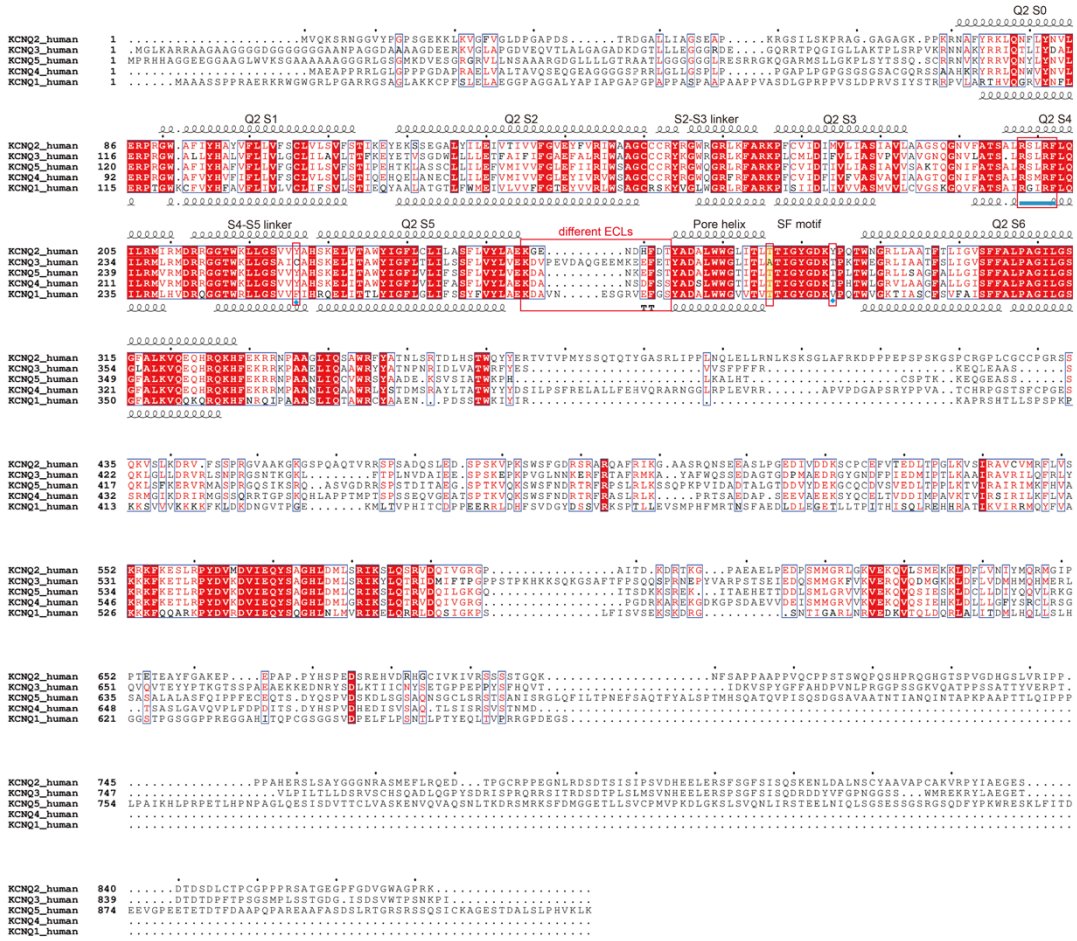

Fig. S1 | Sequence alignment of the human KCNQ family (KCNQ1-5). Aligned sequences of KCNQ1-5 are shown with secondary structural elements for KCNQ2 (*top*) and KCNQ3 (*bottom*, based on the apo M channel structure). Conserved residues (similarity > 0.7) are shaded in red. Subtype-distinguishing residues between KCNQ2 and KCNQ3 are marked with blue squares below the sequences. Conductance-related residues, including KCNQ3 Ala315 and the conserved KCNQ threonine aside the selectivity filter (SF) motif, are shaded in yellow. The elongated loop spanning Arg227-Phe231 on KCNQ3 S4 is highlighted with a blue line. Sequence alignment was performed using ClustalW[1] in MEGA12[2] and visualized with ESPript3.0[3]. Uniport IDs: KCNQ2 (O43526), KCNQ3 (O43525), KCNQ5 (Q9NR82), KCNQ4 (P56696), and KCNQ1 (P51787).

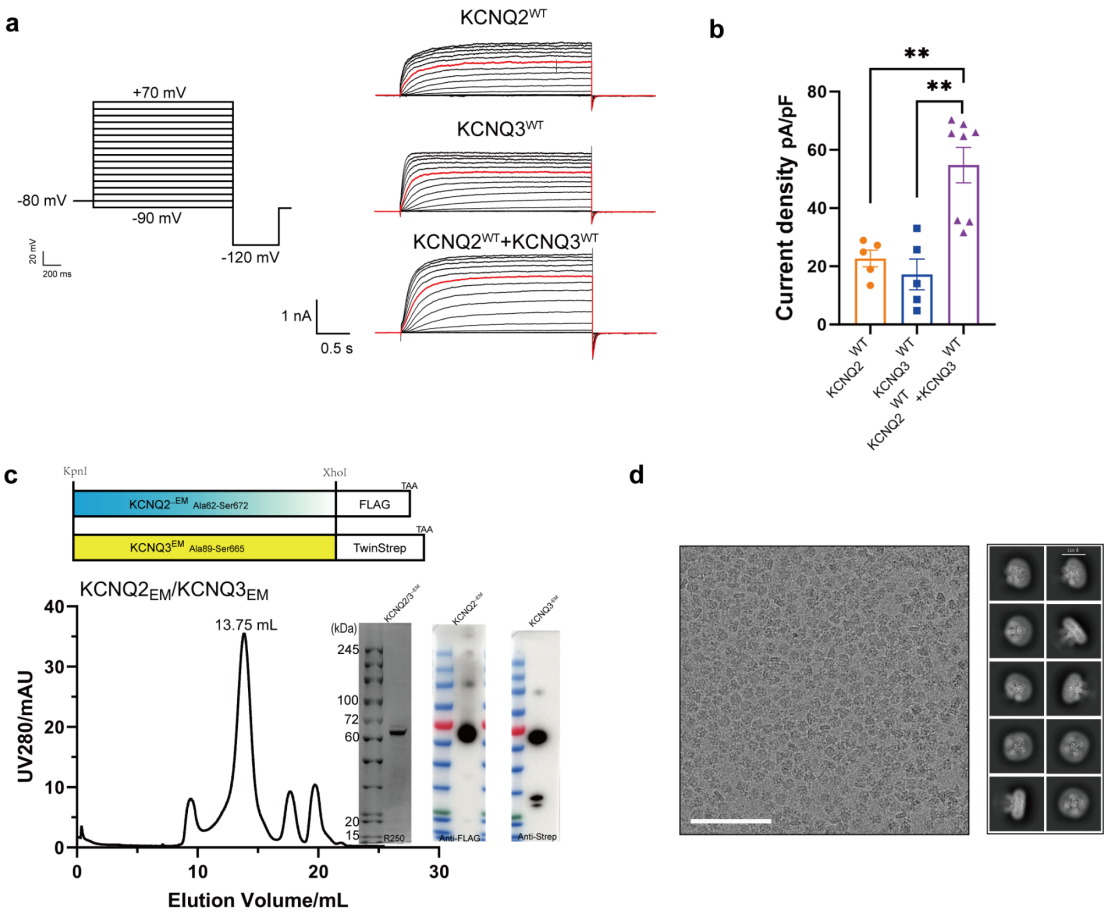

Fig. S2 | Structural and electrophysiological characterization of heteromeric KCNQ2/3 channels and truncated constructs. a, Voltage-clamp protocol and whole-cell patch-clamp recordings of wild-type homo- and heteromeric KCNQ2 and KCNQ3 channels. HEK293T cells were held at -80 mV, followed by 1500-ms depolarizing steps from -90 mV to +70 mV in 10-mV increments, with tail currents obtained by a subsequent 500-ms step to -120 mV. **b,** Current densities of wild-type full-length KCNQ2/3 channels. **c,** Purification of heteromeric KCNQ2/3 complexes. Extracted particles were sequentially applied to anti-FLAG M2 affinity resin and Strep-Tactin Sepharose for two-step affinity purifications, followed by Superose 6 increase 10/300 GL gel filtration. Peak fractions at 13.75 mL were merged and examined by Coomassie blue R250 staining and western blotting to confirm the presence of heteromeric complexes. **d,** Representative cryo-EM micrograph and 2D class averages of KCNQ2/3 particles. Scale bar, 100 nm.

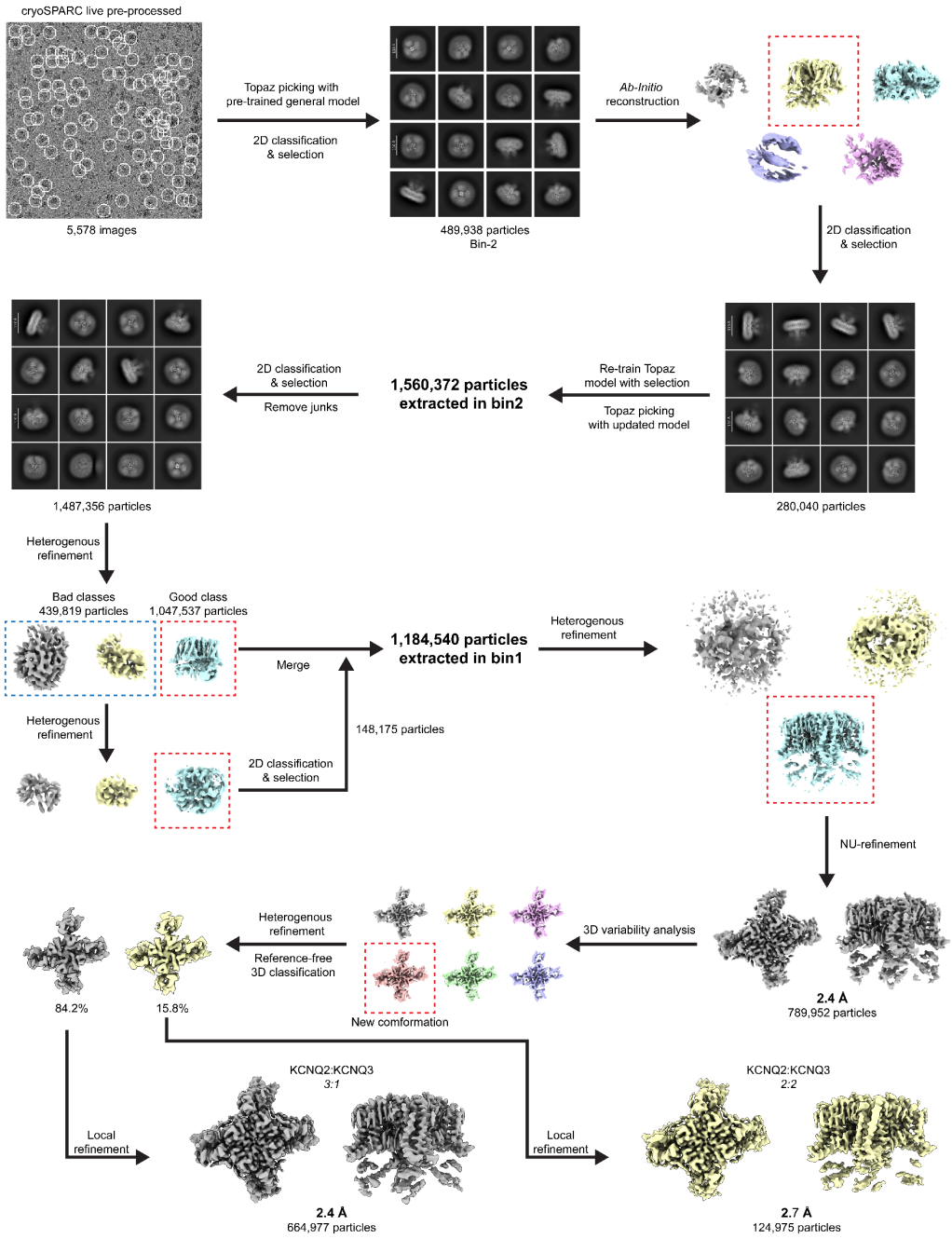

Fig. S3 | Data processing workflow. Please refer to the Methods section for detailed information.

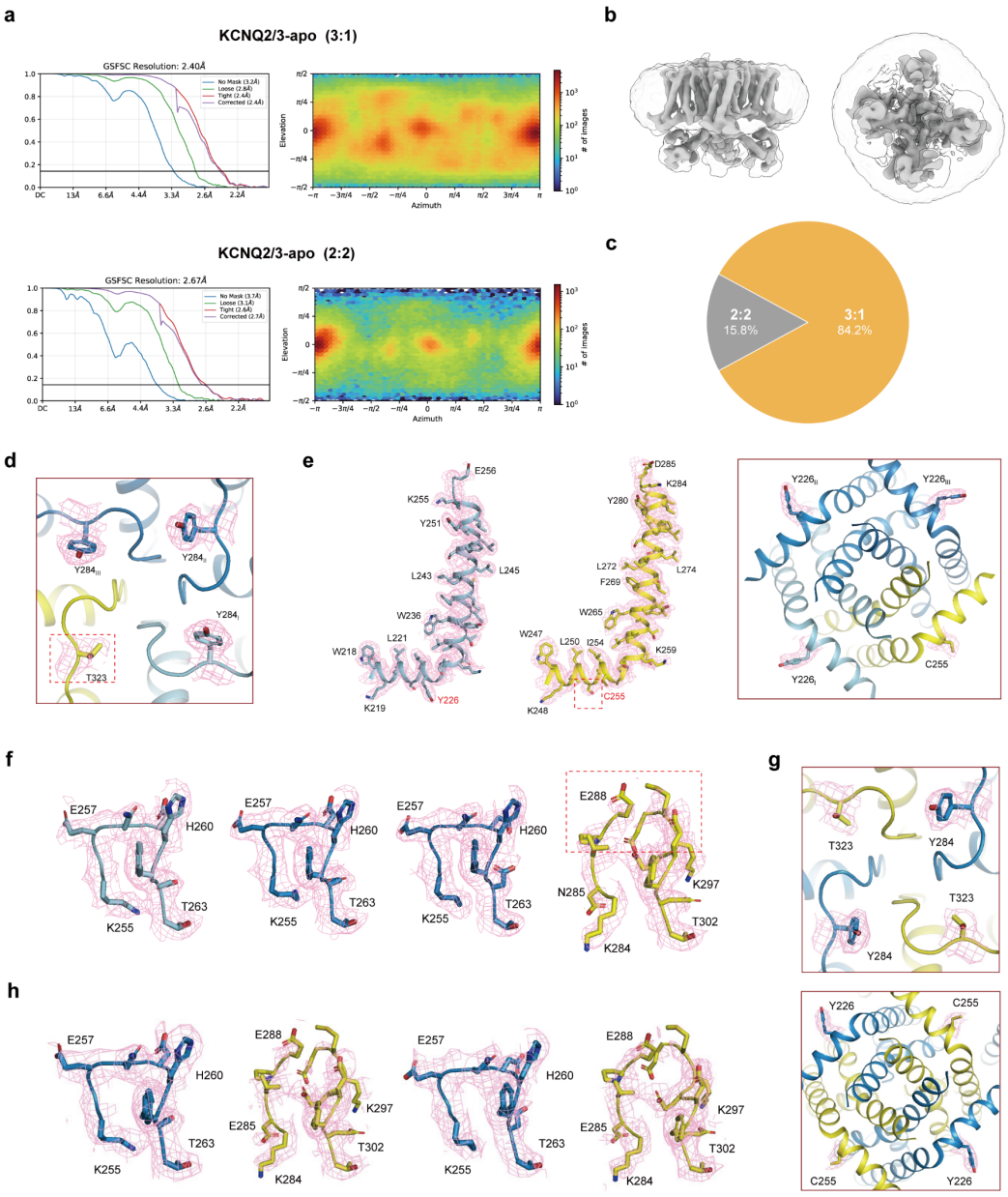

Fig. S4 | Cryo-EM analysis of heteromeric KCNQ2/3 channels. a, Gold-standard Fourier shell correlation (GSFSC) curves and angular distribution assessments for KCNQ2/3 complexes with 3:1 and 2:2 stoichiometries. **b,** Low-pass filtered reconstruction of the 3:1 KCNQ2/3 complex. **c,** Particle distribution within the dataset. **d-f,** Subunit-specific side-chain signatures distinguishing KCNQ3 from KCNQ2 in the asymmetric 3:1 KCNQ2/3 complex, including residues near the extracellular vestibule (Tyr284 in KCNQ2 versus Thr323 in KCNQ3, **d**), residues on the S4-5 linker (Tyr226 in KCNQ2 versus Cys255 in KCNQ3, **e**), and differences in extracellular loops (**f**). KCNQ3-specific features are highlighted in squares. **g-h,** Side-chain signatures distinguishing KCNQ3 from KCNQ2 in the symmetric 2:2 complex.

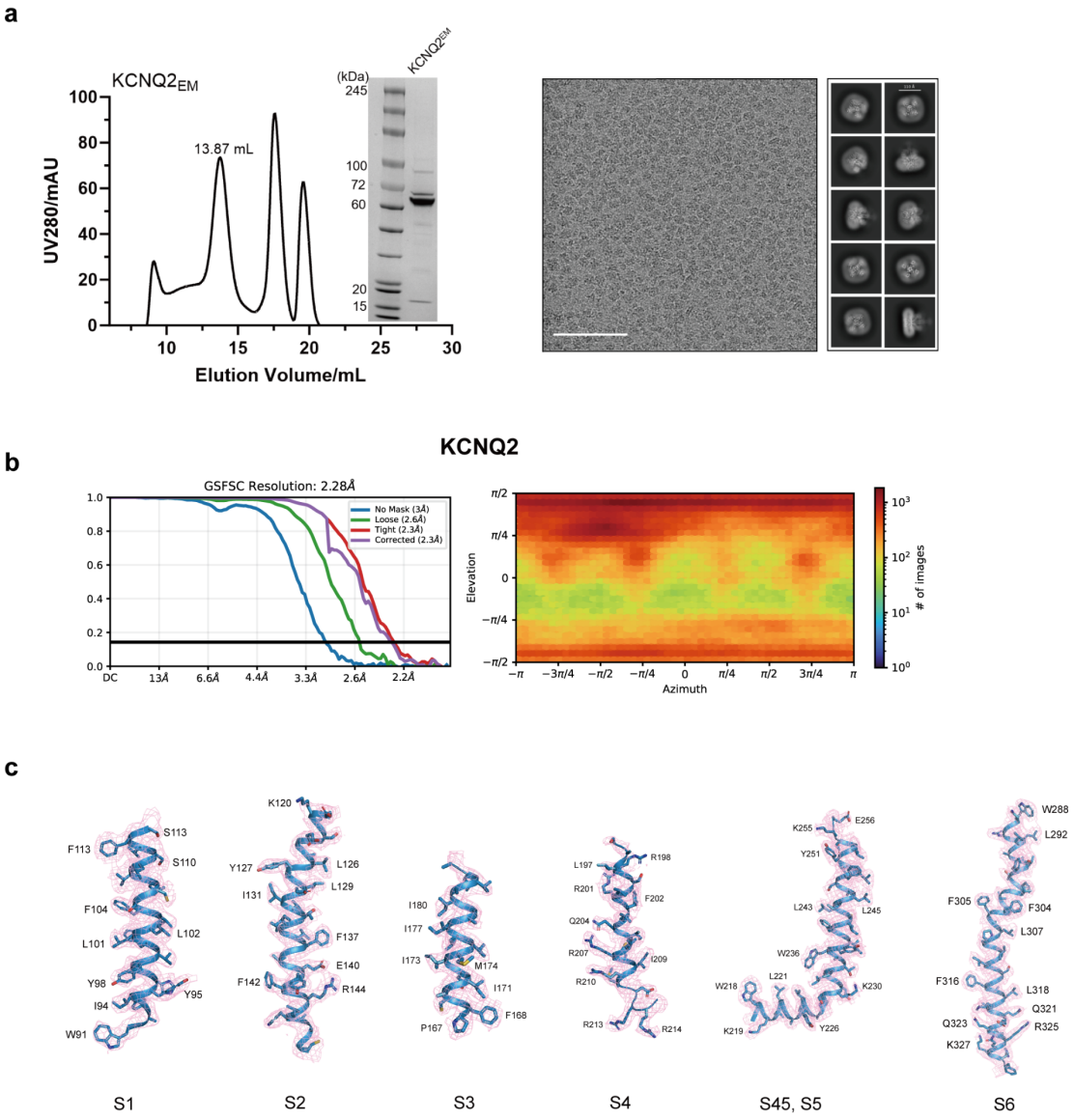

Fig. S5 | Cryo-EM analysis of KCNQ2. a, Protein purification and sample preparation (*left*), with representative micrograph and 2D class averages (*right*). Peak fractions at 13.87 mL were pooled and examined by Coomassie blue R250 staining. **b,** GSFSC curves and angular distribution for homomeric KCNQ2. **c,** Local cryo-EM densities corresponding to signature residues across S1-S6 helices of the KCNQ2 subunit.

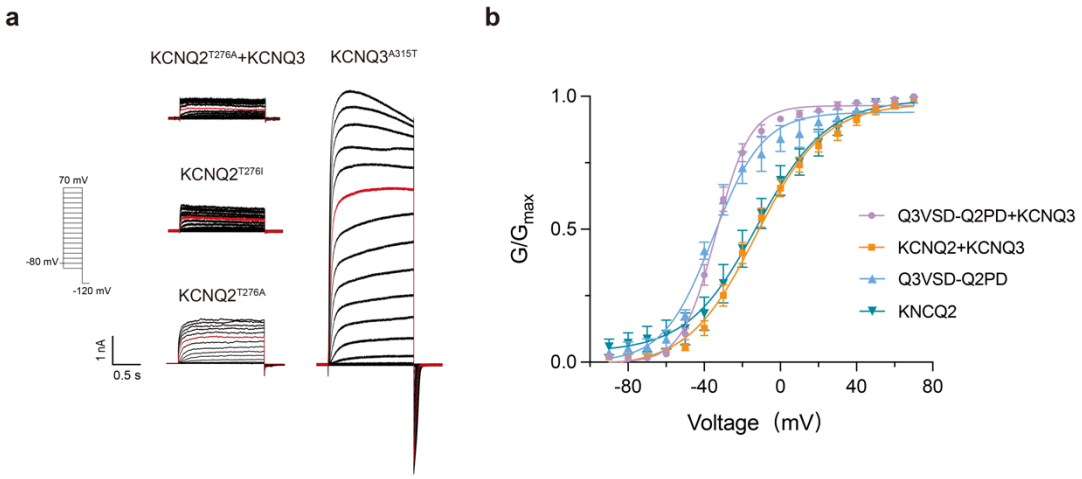

Fig. S6 | Electrophysiological characterization of Ala-substitution and VSD-engineered constructs in KCNQ2/3 channels. a, Representative whole-cell current traces recorded from HEK293T cells expressing KCNQ2^{T276I}, KCNQ2^{T276A}, KCNQ3^{A375T}, and KCNQ2^{T276A}+KCNQ3. **b,** Voltage-dependent activation curves of Q3VSD-Q2PD+KCNQ3, KCNQ2+KCNQ3, Q3VSD-Q2PD alone, and KCNQ2 alone.

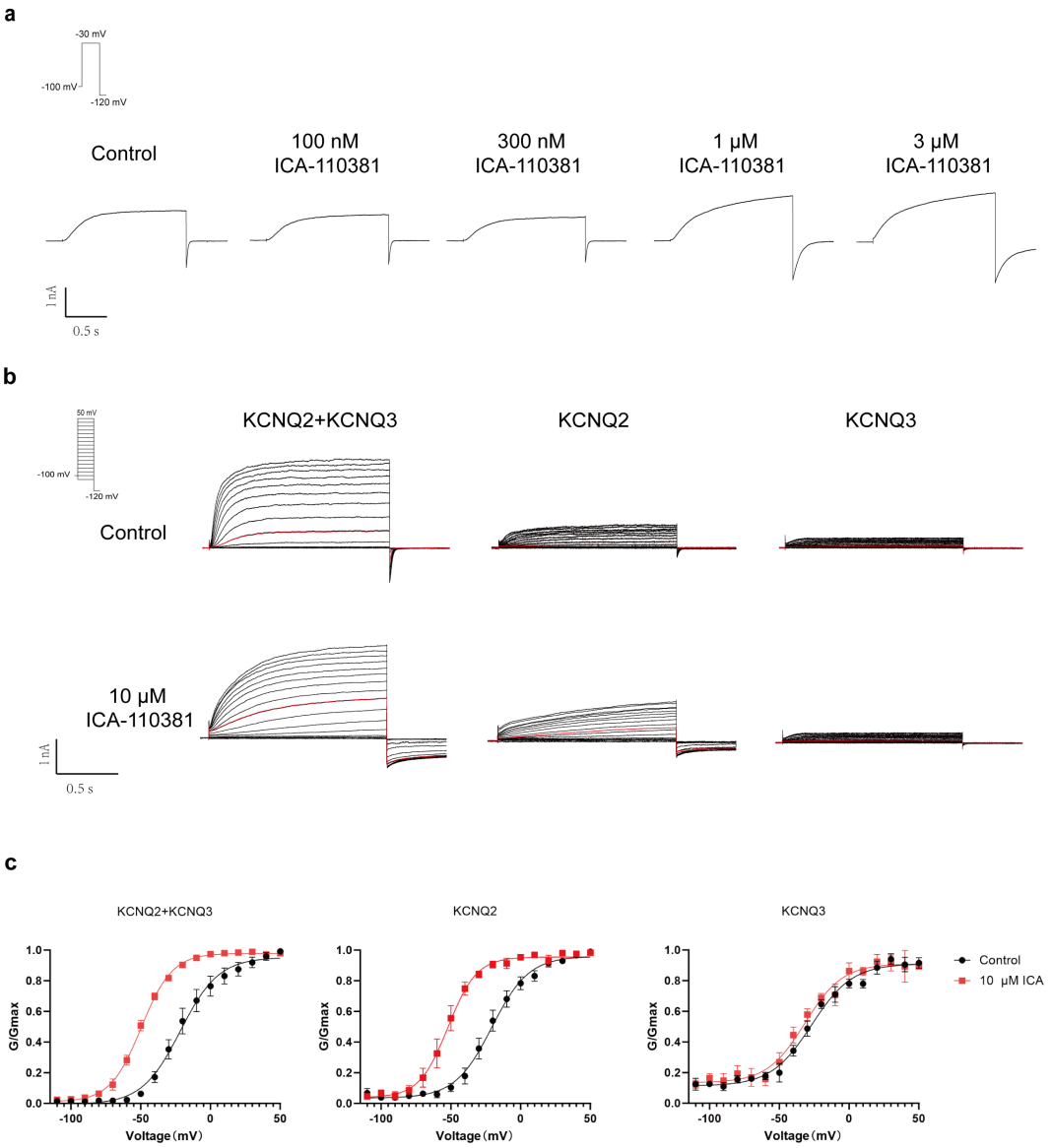

Fig. S7 | Electrophysiological recording for the effects of ICA-110381 on KCNQ2/3. a, Representative whole-cell current traces from heteromeric KCNQ2/3 channels recorded in the presence of varying concentrations of ICA-110381. **b,** Representative current traces from KCNQ2/3, KCNQ2, and KCNQ3 channels in the presence of 10 μM ICA-110381. **c,** Voltage-dependent activation curves of KCNQ2/3, KCNQ2, and KCNQ3 channels in the presence of 10 μM ICA-110381.

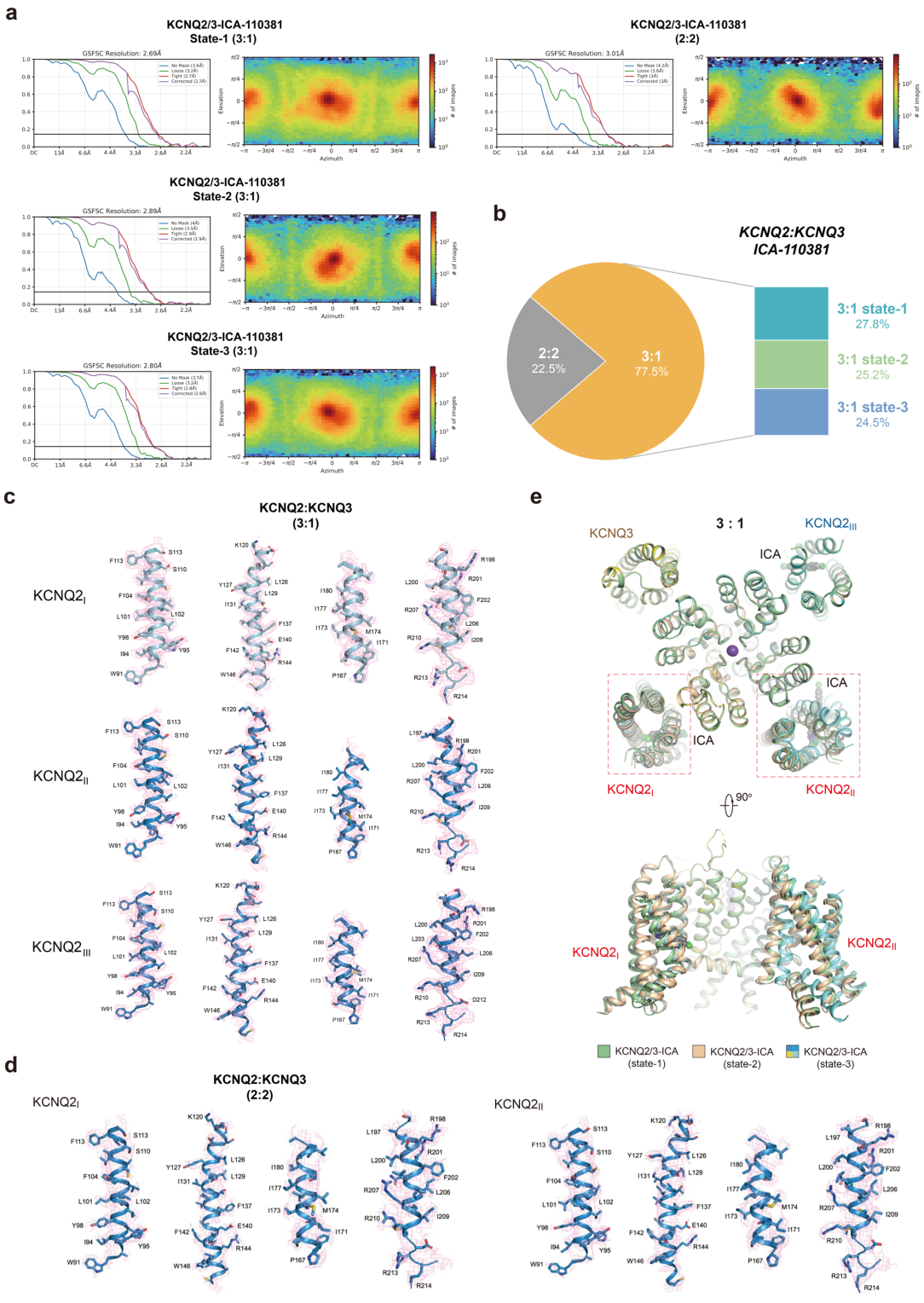

Fig. S8 | Cryo-EM analysis of KCNQ2/3-ICA-110381 complexes. a, GSFSC curves and angular distributions. **b,** Particle distribution within the dataset. **c,** Representative EM density maps for segments involved in ICA-110381 binding in State-3. **d,** Representative EM density maps for segments involved in ICA-110381 binding in the asymmetric 2:2 assembly. **e,** Structural comparison reveals conformational differences

in $KCNQ2_{I}$ and $KCNQ2_{II}$, while $KCNQ2_{III}$ remains largely unchanged upon ICA-110381 binding.

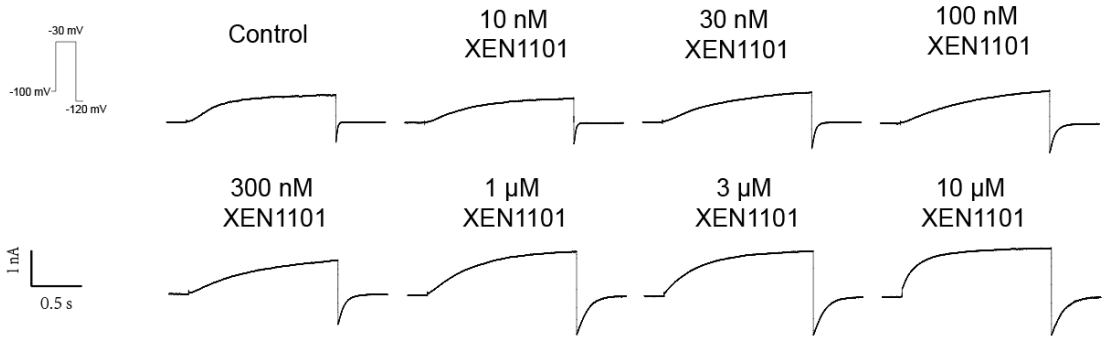

Fig. S9 | Representative current traces from KCNQ2/3 channels recorded under increasing concentrations of XEN1101. Please refer to the Methods section for experimental details.

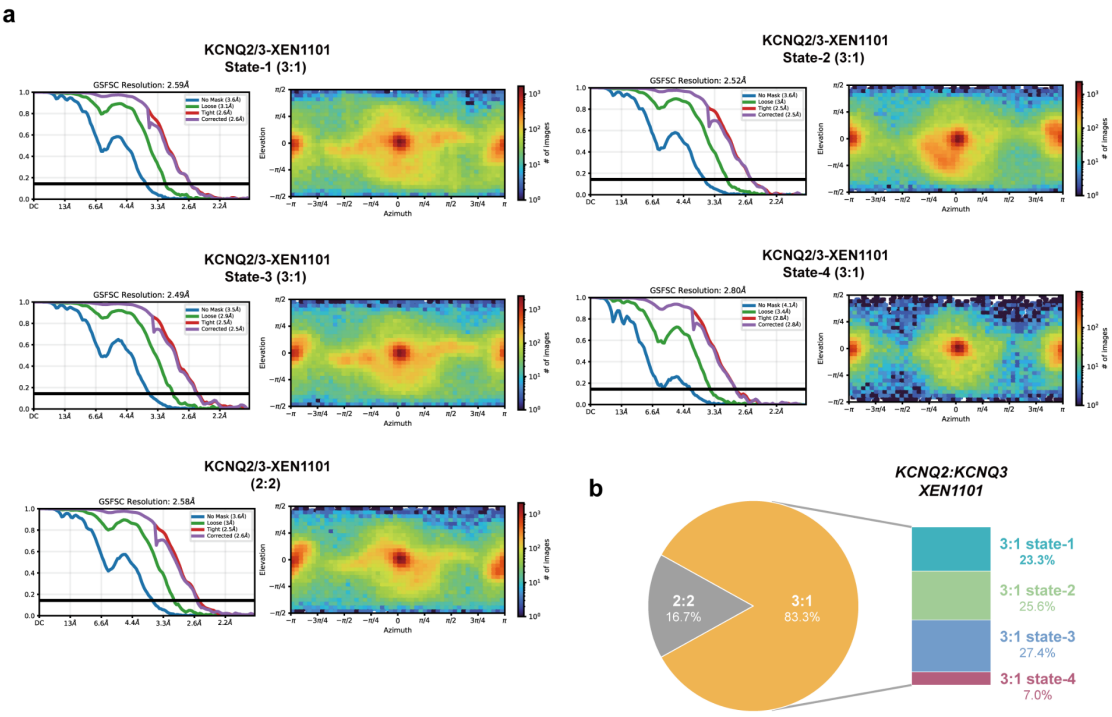

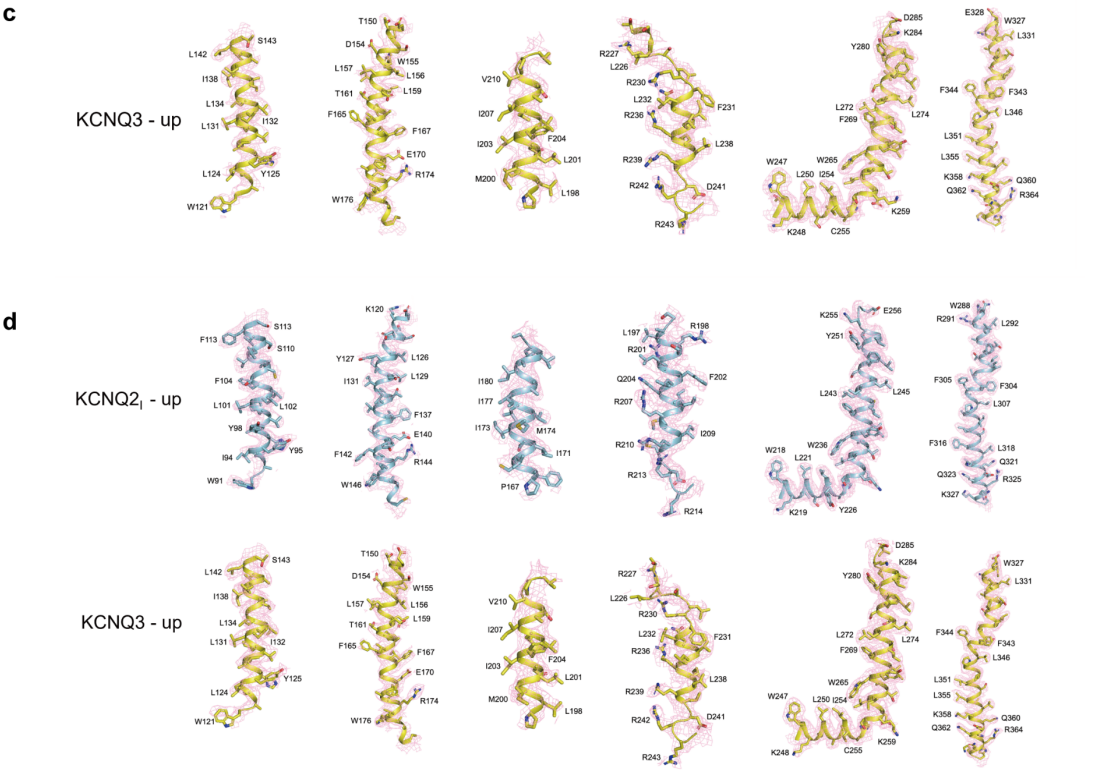

(*to be continued*)

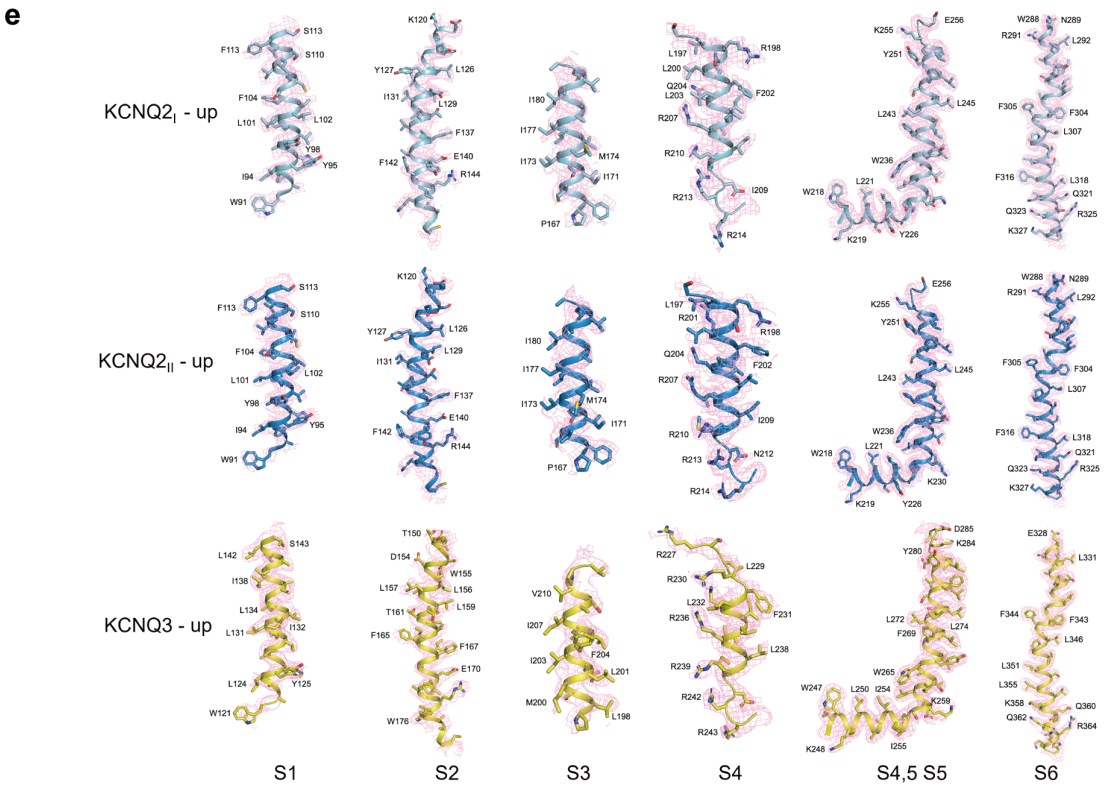

Fig. S10 | Cryo-EM analysis of KCNQ2/3-XEN1101 complexes. a, GSFSC curves and angular distributions. **b,** Particle distribution within the dataset. **c-e,** EM density maps for representative segments of KCNQ2/3-XEN1101 complexes in distinct conformational states.

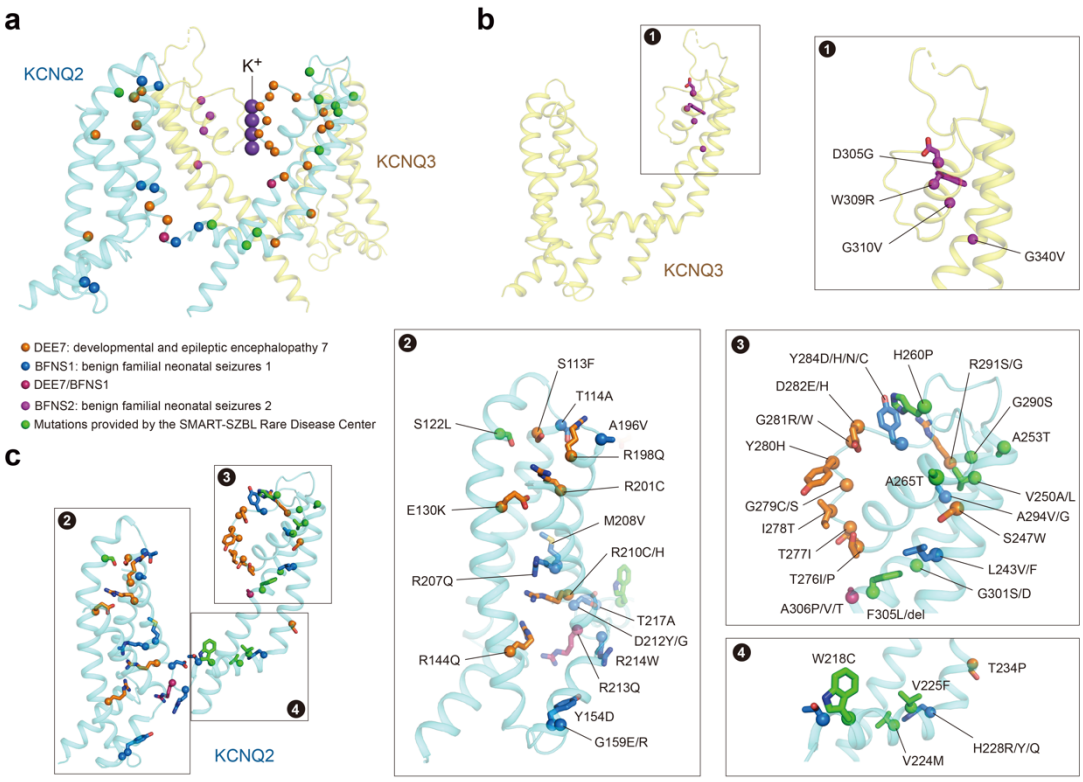

Fig. S11 | Structural mapping of disease-associated mutations in human M-channels. a, Locations of disease-associated mutations mapped onto the structure of the human M-channel. Cα atoms of mutated residues are shown as spheres and color-coded according to disease type. **b-c,** Subunit-specific distribution of disease-associated mutations in the M-channel.

Table S1 | Current densities and activation parameters of wild-type homomeric and heteromeric M-channels.

	Parameters	$KCNQ2^{WT}$+ $KCNQ3^{WT}$	$KCNQ2^{WT}$	$KCNQ3^{WT}$
Tail peak current	Current density (pA/pF)	54.75 ± 6.06	22.69 ± 2.87**	17.2 ± 5.30**
	P	/	0.0022	0.0013
	n	8	5	5
Activation	$V_{1/2}$(mV)	-18.19 ± 1.16	-20.32 ± 1.51	-28.48 ± 2.35****
	P	/	0.2535	<0.0001
	Slope	15.21 ± 1.08	13.10 ± 1.37	13.65 ± 2.11
	P	/	0.2599	0.5245
	n	10	5	5

Statistical significance was defined as $p < 0.05$ (*), $p < 0.01$ (**), $p < 0.001$ (***), and $p < 0.0001$ (****), all relative to the heteromeric KCNQ2/3 condition. Data are presented as mean ± s.e.m., with *n* indicating the number of recorded cells. Values of current density were compared using unpaired *t*-tests, and half-activation voltages ($V_{1/2}$) were analyzed by extra sum-of-squares *F*-tests.

Table S2 | Statistics for cryo-EM data collection and structural refinement.

	KCNQ2/3-apo (3:1)	**KCNQ2/3-apo (2:2)**	**KCNQ2**	**KCNQ2/3-ICA-110381 (3:1)** State-1	**KCNQ2/3-ICA-110381 (3:1)** State-2	**KCNQ2/3-ICA-110381 (3:1)** State-3	**KCNQ2/3-ICA-110381 (2:2)**	**KCNQ2/3-XEN1101 (3:1)** State-1	**KCNQ2/3-XEN1101 (3:1)** State-2	**KCNQ2/3-XEN1101 (3:1)** State-3	**KCNQ2/3-XEN1101 (3:1)** State-4	**KCNQ2/3-XEN1101 (2:2)**
Data collection and processing												
Magnification	130,000	130,000	130,000	130,000	130,000	130,000	130,000	130,000	130,000	130,000	130,000	130,000
Voltage (kV)	300	300	300	300	300	300	300	300	300	300	300	300
Electron dose (e-/Å^2)	50	50	50	50	50	50	50	50	50	50	50	50
Defocus range (μm)	-1.2~-1.6	-1.2~-1.6	-1.2~-1.6	-1.2~-1.6	-1.2~-1.6	-1.2~-1.6	-1.2~-1.6	-1.2~-1.6	-1.2~-1.6	-1.2~-1.6	-1.2~-1.6	-1.2~-1.6
Pixel size (Å)	0.936	0.936	0.936	0.936	0.936	0.936	0.936	0.936	0.936	0.936	0.936	0.936
Symmetry	C1	C1	C4	C1	C1	C1	C1	C1	C1	C1	C1	C1
Total good particle	1,184,540	1,184,540	1,010,784	828,566	828,566	828,566	828,566	1,129,752	1,129,752	1,129,752	1,129,752	1,129,752
Final particles	664,977	124,975	928,950	146,447	132,878	128,963	118,562	171,895	189,473	202,372	51,995	123,746
Map resolution (Å)	2.4	2.7	2.3	2.7	2.9	2.8	3.0	2.6	2.5	2.5	2.8	2.6
FSC threshold	0.143	0.143	0.143	0.143	0.143	0.143	0.143	0.143	0.143	0.143	0.143	0.143
Refinement												
Map sharpening *B* factor (Å^2)	65.0	62.4	72.7	69.1	61.1	72.6	60.4	54.3	51.0	52.0	41.5	53.1
Model composition												
Non-hydrogen atoms	8,084	8,089	8,156	8135	8,135	8,135	8,123	8,191	8,165	8,139	8,191	8,196
Protein residues	996	999	1,000	996	996	996	999	996	993	989	989	999
Ligands	4	4	4	7	7	7	6	7	7	7	7	7
B factors (Å^2)												
Protein	129.64	127.2	82.23	138.13	109.68	109.68	139.36	126.92	116.97	112.65	118.96	130.49
Ligand	92.16	92.16	30.00	159.08	128.28	128.28	159.90	22.04	69.12	57.93	57.93	57.93
R.m.s deviations												
Bond lengths (Å)	0.002	0.003	0.002	0.003	0.003	0.003	0.003	0.003	0.003	0.003	0.003	0.003
Bond angles (°)	0.439	0.473	0.407	0.667	0.546	0.523	0.674	0.475	0.478	0.488	0.549	0.483
Validation												
MolProbity score	1.28	1.33	1.13	1.49	1.44	1.35	1.47	1.14	1.24	1.35	1.32	1.23
Clashscore	5.20	5.97	3.40	9.20	8.04	5.85	8.64	3.52	4.69	4.89	5.81	4.60
Rotamer outliers (%)	0.84	0.48	0.00	0.84	0.84	1.12	0.60	0.84	0.97	1.33	0.85	0.48
CaBLAM outliers (%)	0.94	1.04	0.83	1.25	1.25	1.35	1.36	0.94	1.15	1.15	1.36	0.83
Ramachandran plot												
Favored (%)	99.28	98.88	99.59	99.18	99.18	98.88	99.08	99.49	99.18	99.18	98.87	99.39
Allowed (%)	0.72	1.12	0.41	0.82	0.82	1.12	0.92	0.51	0.82	0.82	1.13	0.61
Disallowed (%)	0.00	0.00	0.00	0.00	0.00	0.00	0.00	0.00	0.00	0.00	0.00	0.00

Table S3 | Summary of disease-associated mutations in KCNQ2 and KCNQ3 subunits.

Mutations	Disease	Structure	Mutations	Disease	Structure
KCNQ2			L268F	DEE7	pore helix
T114A	BFNS1	S1	T274M[4]	DEE7	pore helix
Y154D	BFNS1	S2-3 linker	T276I/P	DEE7	pore helix
G159E/R	BFNS1	S2-3 linker	T277I[4]	DEE7	SF
A196V	BFNS1	S4	I278T[4]	DEE7	SF
R207W	BFNS1	S4	G279C/S[4]	DEE7	SF
R207Q	BFNS1	S4	Y280H[4]	DEE7	SF
M208V	BFNS1	S4	G281R/W[4]	DEE7	SF
D212G[4]	BFNS1	S4	D282E/H[4]	DEE7	P-loop
R213W	BFNS1	S4-5 linker	Y284D/H/N[4]	DEE7	P-loop
R213Q	BFNS1/DEE7	S4-5 linker	R291S/G	DEE7	S6
R214W	BFNS1	S4-5 linker	A294V[4]	DEE7	S6
T217A	BFNS1	S4-5 linker	G301S	DEE7	S6
H228Q	BFNS1	S5	F305del[4]	DEE7	S6
L243F	BFNS1	S5	A306P/V[4]	DEE7	S6
Y284C	BFNS1	P-loop	R333W[4]	DEE7	HA
A294G	BFNS1	S6	P335L[4]	DEE7	HA
A306T	BFNS1	S6	R560W[4]	DEE7	ICL
R333Q	BFNS1	HA	P561S	DEE7	ICL
I341A[5]	BFNS1	HA	V567D[4]	DEE7	HB
W344R[6]	BFNS1	HA	R581Q	DEE7	HB
L351F/V[6]	BFNS1	HA	LL292-293PF[4]	DEE7	S6
R353G	BFNS1	ICL	ML578-579IM	DEE7	HB
S358F	BFNS1	HA	S122L[a]		S2
Y362C[6]	BFNS1	HA	W218C[a]		S4-5 linker
R547W	BFNS1	ICL	V224M[a]		S4-5 linker
R553Q[6]	BFNS1	ICL	V225F[a]		S4-5 linker
K554N	BFNS1/DEE7	ICL	L243V[a]		S5
M578V	BFNS1	HB	V250L[a]		S5
R588S	BFNS1	HB	A253T[a]		S5
L637R	BFNS1	ICL	H260P[a]		ECL
S113F[4]	DEE7	S1	A265T[a]		pore helix
E130K[4]	DEE7	S2	G290S[a]		S6
R144Q[4]	DEE7	S2	G301D[a]		S6
A193D[4]	DEE7	S3-4 linker	F305L[a]		S6
R198Q[4]	DEE7	S4	P561R[a]		ICL

R201C	DEE7	S4	V567F[a]		HB
R210C/H	DEE7	S4	R582Q[a]		HB
D212Y[4]	DEE7	S4	**KCNQ3**		
H228R/Y[4]	DEE7	S5	D305G	BFSN2	pore helix
T234P	DEE7	S5	W309R	BFSN2	pore helix
S247W	DEE7	S5	G310V	BFSN2	pore helix
V250A[4]	DEE7	S5	G340V	BFSN2	S6
N258Y[4]	DEE7	ECL	P574S[7]	BFSN2	HC
D266E	DEE7	pore helix	R780C[7]	BFSN2	CTD

BFNS1: Benign familial neonatal seizures-1; **DEE7**: Developmental and epileptic encephalopathy 7; **BFNS2**: Benign familial neonatal seizures-2.

Structural elements: HA: Helix A; **HB**, Helix B; **HC**, Helix C; **ICL**, Intracellular Loop; **ECL**, Extracellular Loop; **SF**, Selectivity Filter.

Disease mutations in Table S3 are summarized from Uniprot (KCNQ2: https://www.uniprot.org/uniprotkb/O43526/entry; KCNQ3: https://www.uniprot.org/uniprotkb/O43525/entry), [a]data provided by the SMART-SZBL Rare Disease Center, and literatures[4-7].

Reference

1 Hung, J. H. & Weng, Z. Sequence Alignment and Homology Search with BLAST and ClustalW. *Cold Spring Harb Protoc* **2016** (2016). https://doi.org/10.1101/pdb.prot093088

2 Kumar, S. *et al.* MEGA12: Molecular Evolutionary Genetic Analysis Version 12 for Adaptive and Green Computing. *Mol Biol Evol* **41** (2024). https://doi.org/10.1093/molbev/msae263

3 Gouet, P., Courcelle, E., Stuart, D. I. & Metoz, F. ESPript: analysis of multiple sequence alignments in PostScript. *Bioinformatics* **15**, 305-308 (1999). https://doi.org/10.1093/bioinformatics/15.4.305

4 Liu, W. & Devaux, J. J. Calmodulin orchestrates the heteromeric assembly and the trafficking of KCNQ2/3 (Kv7.2/3) channels in neurons. *Mol Cell Neurosci* **58**, 40-52 (2014). https://doi.org/10.1016/j.mcn.2013.12.005

5 Ambrosino, P. *et al.* Epilepsy-causing mutations in Kv7.2 C-terminus affect binding and functional modulation by calmodulin. *Biochim Biophys Acta* **1852**, 1856-1866 (2015). https://doi.org/10.1016/j.bbadis.2015.06.012

6 Miceli, F. *et al.* A Novel Kv7.3 Variant in the Voltage-Sensing S(4) Segment in a Family With Benign Neonatal Epilepsy: Functional Characterization and in vitro Rescue by beta-Hydroxybutyrate. *Front Physiol* **11**, 1040 (2020). https://doi.org/10.3389/fphys.2020.01040

7 Vanoye, C. G. *et al.* High-throughput evaluation of epilepsy-associated KCNQ2 variants reveals functional and pharmacological heterogeneity. *JCI Insight* **7** (2022). https://doi.org/10.1172/jci.insight.156314